www.acsnano.org

Disentangling Electronic Transport and Hysteresis at Individual Grain Boundaries in Hybrid Perovskites via Automated Scanning **Probe Microscopy**

Yongtao Liu,* Jonghee Yang, Benjamin J. Lawrie, Kyle P. Kelley, Maxim Ziatdinov, Sergei V. Kalinin,* and Mahshid Ahmadi*



Downloaded via UNIV OF TENNESSEE KNOXVILLE on April 15, 2024 at 16:29:29 (UTC). See https://pubs.acs.org/sharingguidelines for options on how to legitimately share published articles.

Cite This: ACS Nano 2023, 17, 9647-9657



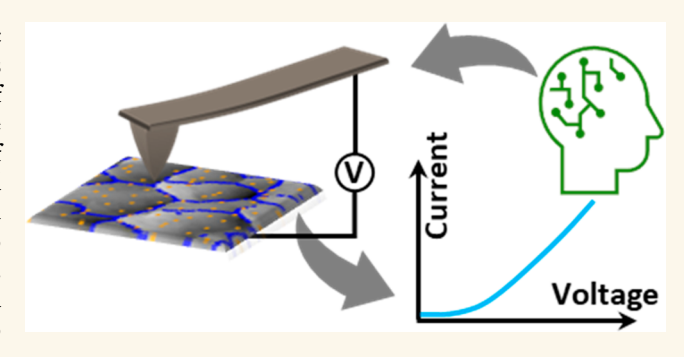
ACCESS

III Metrics & More

Article Recommendations

Supporting Information

ABSTRACT: Underlying the rapidly increasing photovoltaic efficiency and stability of metal halide perovskites (MHPs) is the advancement in the understanding of the microstructure of polycrystalline MHP thin film. Over the past decade, intense efforts have been aimed at understanding the effect of microstructures on MHP properties, including chemical heterogeneity, strain disorder, phase impurity, etc. It has been found that grain and grain boundary (GB) are tightly related to lots of microscale and nanoscale behavior in MHP thin films. Atomic force microscopy (AFM) is widely used to observe grain and boundary structures in topography and subsequently to study the correlative surface potential and conductivity of these



structures. For now, most AFM measurements have been performed in imaging mode to study the static behavior; in contrast, AFM spectroscopy mode allows us to investigate the dynamic behavior of materials, e.g., conductivity under sweeping voltage. However, a major limitation of AFM spectroscopy measurements is that they require manual operation by human operators, and as such only limited data can be obtained, hindering systematic investigations of these microstructures. In this work, we designed a workflow combining the conductive AFM measurement with a machine learning (ML) algorithm to systematically investigate grain boundaries in MHPs. The trained ML model can extract GBs locations from the topography image, and the workflow drives the AFM probe to each GB location to perform a current-voltage (IV) curve automatically. Then, we are able to have IV curves at all GB locations, allowing us to systematically understand the property of GBs. Using this method, we discovered that the GB junction points are less conductive, potentially more photoactive, and can play critical roles in MHP stability, while most previous works only focused on the difference between GB and grains.

KEYWORDS: autonomous and automated experiments, scanning probe microscopy, hybrid perovskites, grain boundary, machine learning

etal halide perovskites (MHPs) have become the most promising class of materials for the next generation of photovoltaic technology due to their rapidly increasing photovoltaic efficiency and low-cost manufacturing. In about a decade of development, the photovoltaic power conversion efficiency (PCE) of single junction and tandem MHP solar cells has surpassed 25% and 31%, respectively, comparable to silicon solar cells that underwent a much longer time period of development.¹ From the perspective of commercializing MHP photovoltaics, further research efforts are dedicated to boosting photovoltaic efficiency and improving the stability of MHP solar cells.²⁻⁴ Underlying the rapidly increasing photovoltaic efficiency and

stability is the advance in understanding of the microstructures of polycrystalline MHP thin films.⁵⁻⁷ As such, intense efforts have been aimed at elucidating the effect of microstructures on MHP properties.^{8–16}

Microscale and nanoscale chemical heterogeneity has proven to be critical to microscale MHP behavior. Using synchrotron

Received: April 13, 2023 Accepted: May 2, 2023 Published: May 8, 2023





X-ray fluorescence microscopy, it was revealed that halide homogenization (in contrast to halide segregation at the micrometer scale) upon the addition of cesium iodide in mixed halide and mixed cation MHPs results in spatially homogeneous photogenerated carrier dynamics and long charge carrier lifetime, along with improved photovoltaic efficiency. 17 Multimodal microscopy measurements revealed that nanoscale compositional disorder can lead to electronic disorder and charge carrier funneling, which ultimately dominates the local optoelectronic response.7 In addition, it was shown that nanoscale phase impurities act as both traps for photogenerated charge carriers and sites of photochemical degradation.⁶ Studies with secondary ion mass spectrometry unveiled the micrometer level chemical redistribution and degradation under light and an electric field, which affects the surface potential and electrical current in the MHP films. 18-22

Grain structure and local strain gradients have also proven to substantially affect MHP optoelectronic properties. Crystallographic twin domains in MHPs have been intensively investigated with electron microscopy, ²³ scanning probe microscopy, ^{12,24–28} and optical microscopy. ^{29,30} The crystallographic difference between adjacent domains was revealed by both transmission electron microscopy and electron backscatter diffraction. 23,31 There still is controversy over whether this twin domain structure is a ferroelectric domain or not and how it affects the optoelectronic behavior of the materials. Theoretical simulations have shown the effect of such domain structures based on both the ferroelectric nature and ferroelastic nature. In investigations with scanning photocurrent microscopy, it was shown that such twin structures potentially do not affect the charge carrier transport.²⁹ In contrast, confocal photoluminescence (PL) microscopy indicates the PL intensity variation between adjacent domains, which was attributed to the difference in local charge carrier concentration.^{29,32} In addition, PL microscopies have shown that the domain walls can act as shallow energetic barriers to delay charge carrier diffusion.¹³ A structure akin to the twin domain is the subgrain boundary, which provides nonradiative recombination sites and restricts carrier diffusion.³³

Understanding the chemical heterogeneity and crystallographic behavior in perovskite grains and grain boundaries is critical to the development of MHP solar cells with high efficiency and stability. Photovoltaic efficiency is determined by photocarrier generation and transport, and grain boundaries can serve as energy barriers and recombination sites that influence charge carrier transport and recombination. The stability of MHP solar cells is determined by both intrinsic material properties and extrinsic effects.^{34,35} One intrinsic property that affects MHP stability is ion migration. 36,37 Thus, grain boundaries acting as ion migration highways play crucial roles in MHP stability. Extrinsic effects such as moisture and oxygen can penetrate into MHP films through grain boundaries and ultimately decompose MHP films. It has been suggested earlier that the GBs are detrimental to photovoltaic performance.³⁸ In contrast, some works also suggested that GBs can be benign,³⁹ but the defects near GBs are detrimental. 40,41 Until now, various approaches have been employed to passivate GBs so as to boost the photovoltaic efficiency of MHPs, including using organic small molecules, 42,43 polymers, 44 metal cations, 45,46 quantum dots, 47 etc.

Two popular tools for investigating grain boundary are scanning electron microscopy (SEM) and atomic force microscopy (AFM). SEM can be used for preliminary

observations of grain and grain boundary structures, and grain size and boundary density are usually linked to photovoltaic device performance. AFM, particularly functional AFM such as Kelvin probe force microscopy (KPFM) and conductive AFM (cAFM), can be used to observe grain and boundary structures in topography and to perform correlative studies of surface potential and conductivity of these structures. For instance, research combining KPFM and cAFM revealed spatial heterogeneity in short-circuit current and open-circuit voltage correlated with different crystal facets within individual grains, implying a direct impact of grain facets on photovoltaic efficiency.⁴⁸ KPFM studies showed charge accumulation at grain boundaries. 39,49,50 Tomographic and conductive AFM has revealed grain boundaries as highly interconnected conducting channels for carrier transport.⁵¹ However, most AFM measurements on MHP have been performed in the imaging mode, and they have provided information only at a static condition. AFM spectroscopy mode allows us to investigate the dynamic behavior of materials, e.g., conductivity under sweeping voltage, aka current-voltage curves.

Until now, AFM spectroscopy measurements have been limited by manual operation by human operators. For instance, an AFM probe can be manually positioned at a grain or a grain boundary to perform current—voltage measurements. As a result, only very limited data have been obtained, and systematic investigations of objects of interest (e.g., mapping current—voltage measurements across a complete grain boundary) have been virtually impossible. Recently, we developed a deep convolutional neural network (DCNN) with a combination of a holistically nested edge detector and a deep residue learning framework to convert raw microscopy images into the segmented image showing objects of interest (e.g., convert topography image to grain boundary image). Implementing this DCNN in an operating AFM will allow us to convert stream data to a segmented objects-of-interest image.

Here, we designed a workflow combining the conductive AFM measurement with above-described DCNN to systematically investigate grain boundaries in MHPs. We trained the DCNN with preacquired data to convert a topography image to a grain boundary (GB) image. In this work, the source training data include two MHP SPM images with 256×256 pixels, and the training data set with a size of 250×250 pixels is extracted from these source images. The training data set was divided into a training set and a verification set with a ratio of 80%:20%. Then, the coordinates of GBs can be extracted from the GB image, and the workflow drives the AFM probe to each GB coordinate and performs a current—voltage curve (IV) in an automated manner without human intervention. At the end, the results including IV curves at all GB locations allow us to systematically understand the property of GBs.

RESULTS AND DISCUSSION

As a model system, a state-of-the-art mixed formamidinium (FA) and cesium (Cs) cation (FACs) MHP (FACs-MHP), with 17% Cs composition ratio, is selected for this measurement. Mixed FA and Cs MHPs show excellent phase stability compared to the MHPs with volatile methylammonium (the MHP structures are compromised upon methylammonium evaporation), and a PCE of 22.7% has been reported for FACs-MHPs. ^{54,55}

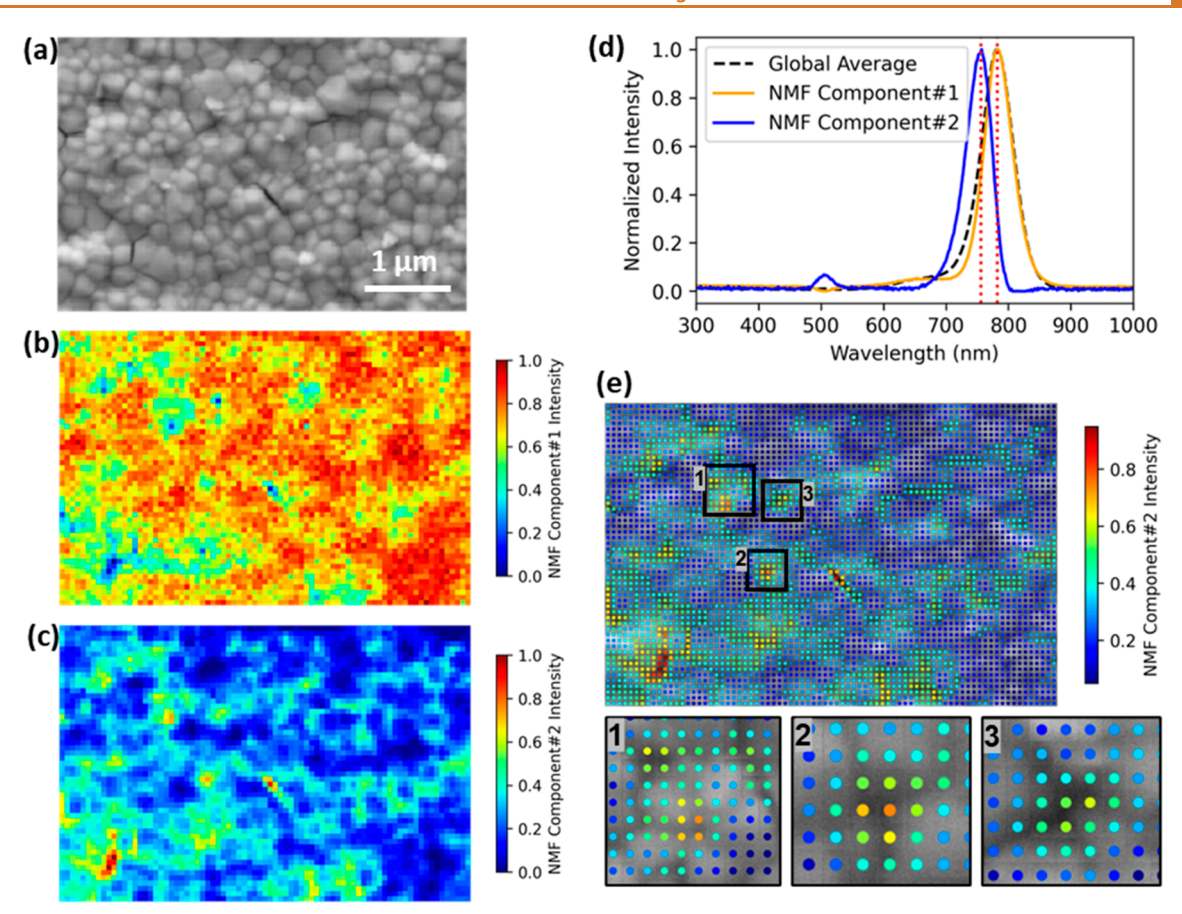


Figure 1. CL results. (a) SEM image shown the grain and GBs structures. (b-c) Images of NMF component #1 and #2, respectively. (d) NMF component #1 and #2 spectral compared to the global average spectrum. (e) NMF component #2 distribution map over the SEM image, where we show three enlarged images indicating the higher component #2 intensity at GB junction points.

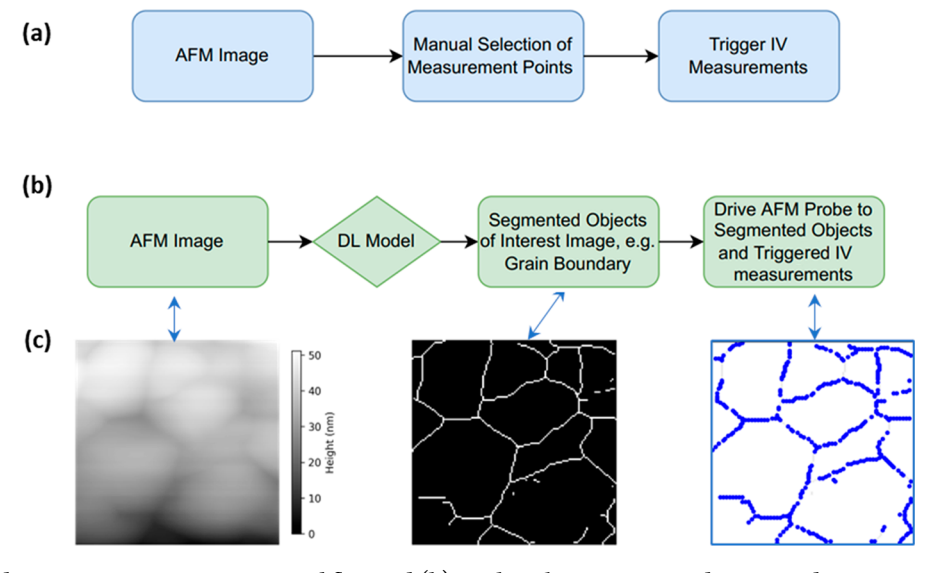


Figure 2. (a) Standard spectroscopy measurement workflow and (b) machine learning powered automated spectroscopy measurement (AE) workflow. The advantages of AE compared to standard method are, for instance, shown in (c). AE can perform IV in all blue points shown in (c), but we can measure only a few points in the standard method.

To assess the spatial heterogeneity of the MHP film, we performed hyperspectral cathodoluminescence (CL) microscopy first. Shown in Figure 1a is a scanning electron microscopy (SEM) image obtained during the CL measurement, in which grain and GB structures are visible. The local CL spectra, with a 60 nm pixel size, are simultaneously

collected, and the hyperspectral CL image illustrates the spatial optoelectronic properties of this region. We performed nonnegative matrix factorization (NMF) to decompose the properties encoded in the CL spectra, revealing local electronic features. Using five components, key spectral features and associated CL maps are successfully disentangled (as shown in

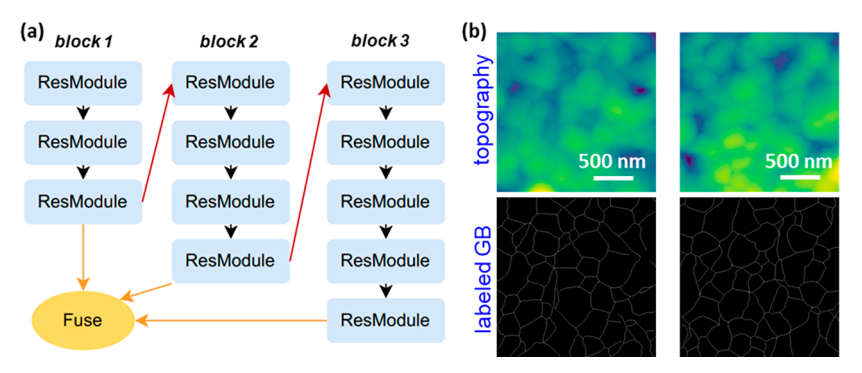


Figure 3. (a) ResHedNet network, where red arrows represent Max Pool, dark arrows represent Relu Activation, and orange arrows represent transfer of tensors. The training in this work was done using focal loss. (b) The topography images and corresponding labeled GB images for training the ResHedNet network.

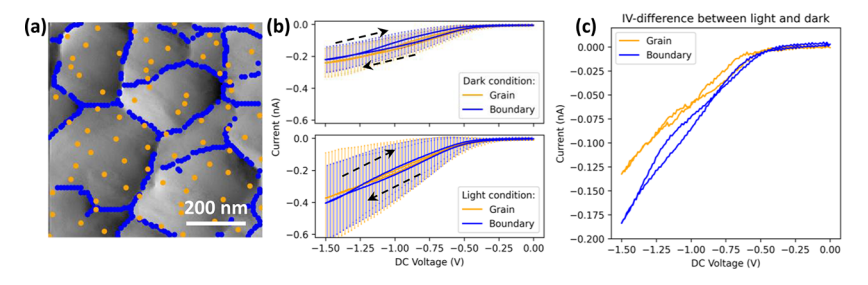


Figure 4. (a) ResHedNet predicted grain boundary locations shown as blue points, and IV measurements were performed at grain boundary (blue points) automatically. We modified the workflow to perform IV in grain as well, shown as orange points. (b) Average IV response from grain boundary (blue) and grain (orange), under dark conditions (top) and light conditions (bottom). (c) The difference in IV between light conditions and dark conditions.

Figure S1). We find that component #1 and component #2 likely correlate to CL emission at grains and GBs including junction points, respectively. These decomposed CL maps are shown in Figure 1b,c, and the corresponding CL spectra of both components, as well as the global-averaged CL spectrum, are shown in Figure 1d. The CL spectrum of component #1 exhibits a main peak centered at 783 nm, consistent with the global averaged spectrum. The CL spectrum of component #2 includes a main peak around 756 nm (18 nm blue-shifted from the global average), indicating a slightly larger bandgap at these regions compared to that of grains. The spectrum also contains another small peak at around 505 nm, suggesting component #2 which is attributed to decomposed PbI₂ luminescence. Moreover, it is obvious that the intensity of component #2 is higher at GBs and possibly even higher at some junction points, as shown in Figure 1e.

The above results led us to investigating the electronic properties of junction points. Various microscopes are known as powerful tools for nanoscale characterization; for instance, we can conduct cAFM to study the nanoscale conductivity of functional materials. cAFM can be run in image mode and spectroscopy mode. In the image mode, we apply a DC voltage through the AFM tip and probe the current at each pixel. This allows us to obtain a current map showing the conductivity of the measured regions. In spectroscopy model, we can move the probe to the location of interest and apply a DC waveform to probe the current-voltage (IV) curve, and the IV curve can offer more details about the sample. However, the limitations of these standard microscopic measurements are that the image mode allows us to find the conductivity only under a static condition, i.e., under a specific DC voltage; the spectroscopy mode requires manual operation to select the measurement pixels (as shown in Figure 2a), which is

monotonous and time-consuming. Traditionally, we are also able to perform grid spectroscopy measurements (e.g., shown in Figure 1 of CL grid spectroscopy measurements). However, in such grid spectroscopy measurements, the measurement points do not necessarily fall on the object of interests. In addition, a dense grid spectroscopy takes too long and potentially results in material damage or degradation. Therefore, it necessitates a method that allows us to perform spectroscopy measurements on the objects of interest.

In this regard, we developed a workflow powered by deep learning (DL) that enables an automated study of IV behavior of specific objects in microscopy images. As shown in Figure 2b,c, this workflow includes a ML model that converts a stream AFM image to segmented objects of interest. The coordinates of these objects can be extracted from this object image and transferred to AFM, and in doing so, the microscope performs IV measurements at all coordinates. An example is shown in Figure 2c, a topography image can be converted to a grain boundary image, where the grain boundary is the object of interest here; then, the coordinates of grain boundaries are shown as the blue spots, and IV measurements will be performed at these blue spots.

The DL model in the workflow is based on the modified version of a holistically nested edge detector⁵⁶ augmented with residual connections. The original holistically nested edge detector contains five VGG-style⁵⁷ convolutional blocks, each with a side-output layer allowing learning features at multiple scales, which are fused at the end of the network. However, we found that for standard experimental SPM data, adding more than three convolutional blocks does not improve the domain boundaries detection rate and quality. On the other hand, replacing convolutional layers in each of the three convolutional blocks with a ResNet⁵⁷ module leads to a significant

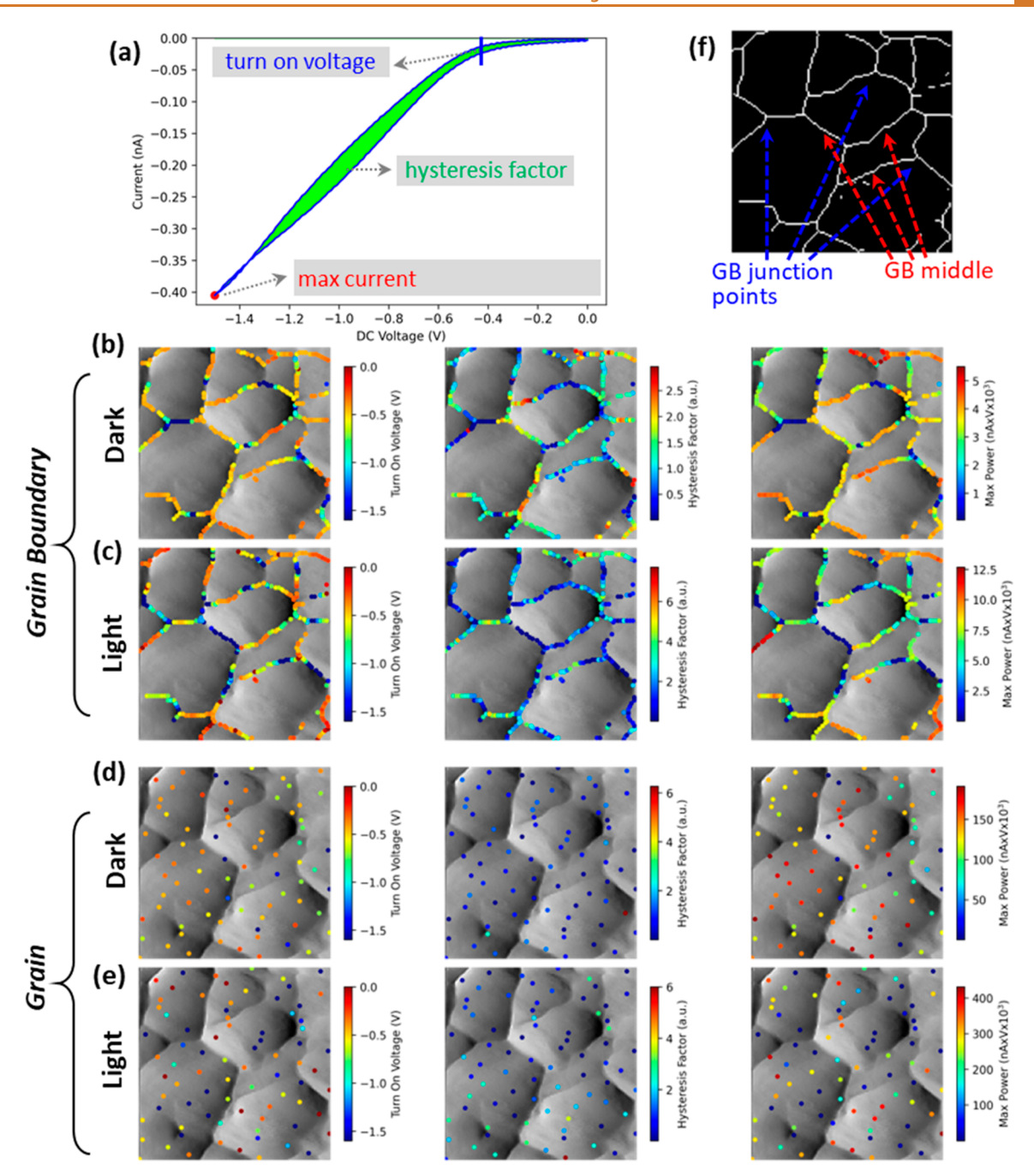


Figure 5. (a) Three physical descriptors are defined; (b-e) shows the distribution of these descriptors as a function of location; (f) indicates GB junction points and GB middle locations.

increase in the accuracy of domain boundaries (or walls) detection, as was demonstrated by some of the authors earlier. ⁵⁸ We call this neural network architecture ResHedNet, as shown in Figure 3a.

Finally, to improve the robustness of ResHedNet predictions on real-time data streams, we train an ensemble of ResHedNet models with different (pseudo)random initialization of weights and different (pseudo)random shuffling of training data batches. The data used for training the ResHedNet is shown in Figure 3b.

We trained the ResHedNet with the preacquired topography image; the grain boundary (GB) in the topography is labeled with ImageJ for training. The training data are shown in Figure 3b. The training was performed using AtomAI software

package, and the detailed training process can be found in the provided Jupyter Notebook. Next, we implemented the trained ResHedNet model in an operating microscope to convert real-time topography images to GBs images. Then, the IV measurements were performed at GBs and grain locations (which is the reverse of the GB image). As shown in Figure 4a, the blue spots correspond to GBs, and the yellow spots correspond to grains, where IV measurements were performed at each spot in an automated manner. Since MHP is a photovoltaic material, its property alters upon light illumination. Multiple works have indicated that light illumination changes the MHP property via reducing ion migration activation energy, photoinduced strain, phase segregation, etc. ^{18–20,28,59–62} Therefore, we performed IV measurements at

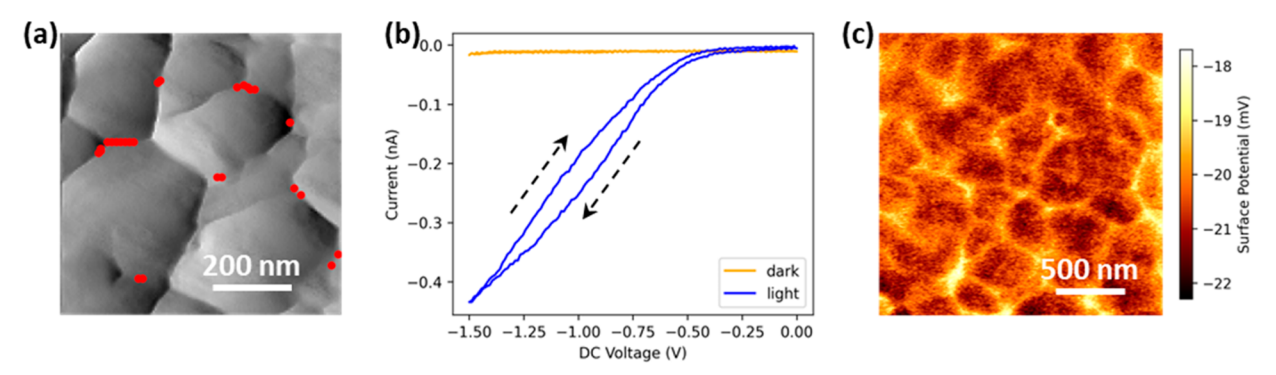


Figure 6. IV curves at junction points. (a) Extract the insulating points under dark conditions, shown in a, and they indeed distribute at junction points. Then, we plot the averaged IV under dark and light conditions, shown in (b). It is seen that these points are insulating under dark and show large hysteresis under light. (c) The KPFM image shows surface potential under dark conditions.

these locations under both dark conditions and light illumination. Here the illuminating light is a built-in LED light in the microscope; its intensity is equivalent to 0.1 sun. Shown in Figure 4b is the averaged IV response under dark conditions at GB and grain. It is observed that the conductivity of GB under light is slightly smaller than grain, while the IV of GB exhibits a larger hysteresis. Under light conditions, shown in Figure 4c the maximum current at -1.5 V indicates that GB is more conductive than grain; nonetheless, the IV hysteresis of GB is still larger.

To check the photoresponse of grain and GB, we also plotted the difference of IV under light and dark in Figure 4d, which are obtained by subtracting dark IV from light IV. The large error bar in Figure 4 implies that the GB behavior can be largely different and highlights the importance of investigating each GB point. Obviously, GB shows a larger IV difference, suggesting that the GBs are more photoresponsive. The discussion of the GB effect on the photovoltaic effect has been controversial; some believe the GB is beneficial for PV effect, while others suggest GB is detrimental. 63,64 Our results show that, on one hand, the GB exhibits a larger photocurrent; on the other hand, GB exhibits larger IV hysteresis. The origin of these phenomena is likely due to ion migration and charge accumulation at GB.65 The charge accumulation leads to a high carrier density at GB under illumination and hence a higher conductivity. Ion migration is due to the higher defect density at GB, and induces larger IV hysteresis under both dark and light. Accordingly, we suggest that the effect of GB cannot be simply evaluated by a higher current, which may mislead us to conclude the beneficial effect of GB. Owing to the systematic investigation of IVs at GB here, we are able to observe the larger IV hysteresis at GB, indicating the detrimental side of GBs.

In addition to comparing the average behavior of GBs and grains, we also explored the IV behavior as a function of location within GB or grain. To do so, we define several physical descriptors to represent the property of the IV curve. As shown in Figure 5a, the turn on voltage represents the voltage where the current starts increasing; the hysteresis factor represents the difference between forward and reverse IVs; the maximum current represents the maximum current under the sweeping voltage. These properties are extracted from each IV curve and plotted as a function of locations. Shown in Figure 5b—c is the distribution of these properties at GBs, where the color represents the magnitude of the corresponding physical descriptors. Interestingly, under dark conditions, the turn on

voltage around the GB junction points is extremely large (dark blue in the first image in Figure 5b). There is also a trend that the turn on voltage gradually increases (from red to cyan) near the junction points. However, the behavior of the turn on voltage is largely different under light as shown in the first image of Figure 5c—the GB junction points mostly do not show the largest turn on voltage now; instead some GB middle (middle of GB) shows large turn on voltage. In the meantime, the GB junction points also show smaller hysteresis and smaller maximum current under dark, while these behaviors of GB junction points are also different under light conditions. In contrast to the clear trend of IV behavior at GB—a strong correlation between IV behavior and locations, and the IV behavior in grains is almost random—no clear correlation between IV behavior and locations, as shown in Figure 5d—e.

To understand the origin of the IV behavior at GB junction points, we checked the exact IV curves at GB junction points. A mask is used to extract the locations with a large turn on voltage under dark conditions (according to our observation in Figure 5b, large turn on voltage locations are near GB junction points), and the extracted locations are shown as red spots in Figure 6a. The corresponding averaged IV curves from these locations are plotted in Figure 6b. It is interesting that these locations are insulating under dark as evidenced by the flat IV curve (yellow curve in Figure 6b). However, these locations become highly conductive under light and exhibit large IV hysteresis (blue curve in Figure 6b).

Inspired by this observation, we further explored the surface potential of this sample by KPFM, in particular, the surface potential of GB junction points. The KPFM result is shown in Figure 6c, and it is seen that GB exhibits a higher surface potential than grains, and the GB junction points exhibit further higher surface potential—higher than the GB middle. This is consistent with our observation in CL measurements, where we found the junction points exhibit a higher intensity of components related to PbI₂. Since PbI₂ is known as a p-type semiconductor, it can lead to a higher surface potential at the GB junction potential. However, several previous works indicated that excess PbI2 in MHP leads to a morphology difference.66-68 In our work, we did not observe a distinct morphology difference, and we suggest that this is most likely because of the small amount of PbI₂ in our film, which may bury in the MHP so that it does not change morphology; nevertheless, it does affect the MHP properties and hence lead to the change in CPD, CL, and conductivity.

To our knowledge, even though GB and grain are extensively investigated, such behavior of GB junction points was not discovered before. Tremendous works indicate that GB affects the degradation of MHP, so here a further question is how the GB junction points affect the stability of MHP. Photovoltaic devices operate under light and an electric field, so it is worth testing the stability of GB junction points under these external fields. Since such a microstructure cannot be tested on the device level, we select the microscope as our tool for a stability study as well. Figure 7a shows the topography

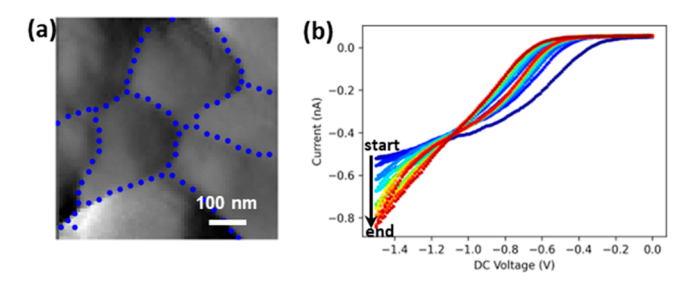


Figure 7. Evolution of IV under continuous sweeping voltages. (a) Topography image and IV measurement points. (b) Averaged IV at GBs.

and GB coordinates for IV measurements. In this stability study, we apply multiple cycles of sweeping voltage waveforms under light conditions, as shown in Figure 7b. We used the evolution of the IV curve as an indicator for stability, and shown in Figure 7c is the evolution of averaged IV curves, where the maximum current at -1.5 V gradually increases as a function of time (from blue to red).

Same as previous analyses, we also extracted the physical descriptors of the turn on voltage, hysteresis factor, and maximum current from the IV curves. Here, in order to show the IV curve change between the beginning and the end, we plotted the difference of physical descriptors between the first cycle and 10th cycle in Figure 8a-c. It is interesting that the turn on voltage at GB junction points almost does not change, indicated as cyan color (difference is 0 V) in Figure 8a. Correspondingly, the difference in hysteresis and maximum current is also near 0. We further created a mask to extract the points with a small difference in the turn on voltage, shown as the blue spots in Figure 8d. It is seen that these spots mostly located near GB junction points. The averaged IV curve from these spots in Figure 8e is shown consecutively. First, we found that the current for these spots (near GB junction points) is smaller than other spots; second, the change of IV curves during continuous sweeping at these spots is also smaller than other spots.

This result indicates that the IV property of these GB junction points is relatively constant than other GB regions, implying that junction points do not induce significant degradation of MHP under light and in an electric field during a short time scale (e.g., here the IV sweep time is only 12 s). This observation is consistent with our hypothesis that there is small amount of PbI₂ buried in MHP at GB junction points—several works have suggested that excess PbI₂ can passivate defects and hence suppress the ion migration, ^{69,70} which results in relatively constant IV at GB junction points. However, the long-term effect of junction points and the composition of junction points on stability needs further investigation; and noteworthily, our CL results indicate a blue-

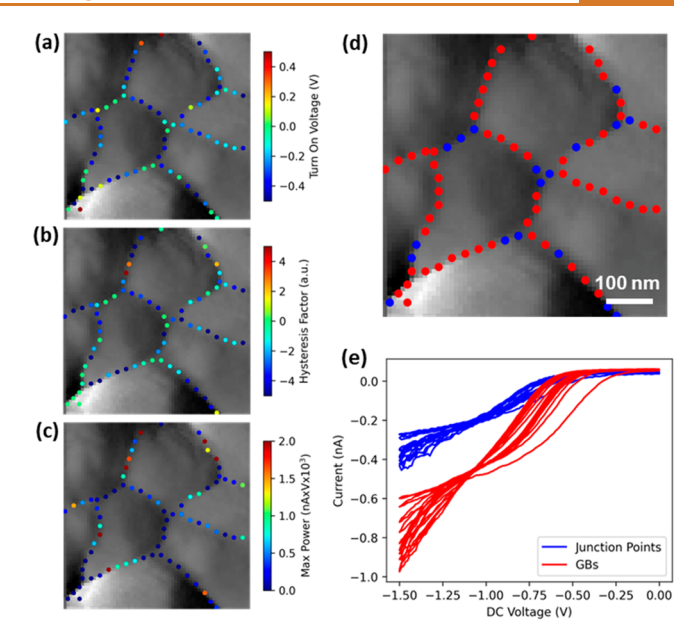


Figure 8. Evolution of IV characteristics under continuous sweeping voltages. (a-c) Evolution of physical descriptors extracted from IV data shown in Figure 7; the difference between first sweep cycle and tenth sweep cycle of (a) turn on voltage, (b) hysteresis, (c) maximum current as a function of location, respectively. (d) Markers of masked small change IV (blue points) and large change IV (red points). (e) Averaged IV corresponding to the markers in (d).

shifted peak near some GB junction points, and such a blue-shifted peak was attributed to a partially decomposed intermediate phase. Nonetheless, in both cases, our study here suggested that the GB junction points can play critical roles in MHP stability.

CONCLUSIONS

In summary, we developed an automated conductive atomic force microscopy approach for investigating the local conductivity of functional materials. This approach combines the power of machine learning and AFM. We used this approach to study an MHP thin film. We revealed the behavior of GB junction points in MHP film, which are insulating under dark conditions and exhibit larger current-voltage hysteresis under light conditions. Combined with CL measurements and KPFM measurements, we showed that the junction points have higher PbI₂ composition and hence higher surface potential. Our IV measurements suggest that the junction points are more photoactive and do not lead to significant degradation of MHP in a short time scale. This work highlights the role of GB junction points, while most previous works only focused on GB and grains. In addition, the developed automated microscopy can be universally used for investigations of other functional materials.

EXPERIMENTAL SECTION

MHP Synthesis. 1.0 M of $Cs_{0.17}FA_{0.83}PbI_3$ perovskite precursor solution was prepared by dissolving a mixture of respective volumetric amounts of FAPbI₃ and CsPbI₃ in a mixed solvent of DMF and DMSO [DMF (v): DMSO (v) = 5:1] in a N₂ glovebox. The solution was spin-coated on the ITO substrates with a two-step process for making the film; 500 rpm 10 s (1000 rpm/s) followed by 4000 rpm 35 s (2000 rpm/s), with the perovskite solution added before spin-

ACS Nano www.acsnano.org Article

coating. Chlorobenzene was gently added 10 s before the end of the second step. The films were then annealed at 150 $^{\circ}\mathrm{C}$ for 10 min.

Hyperspectral CL Microscopy. A FEI Quattro SEM instrument with a Delmic Sparc CL collection module, utilizing a parabolic mirror to collect the CL signals was used. An electron beam with an acceleration voltage of 5 kV (with a beam current of 32 pA) was passed through a hole in the parabolic mirror for sample excitation, with an acquisition time of 400 ms per CL spectrum with a 60 nm size pixel; CL spectra were collected by scanning across the fixed area (defined with a size of 79×53 pixels). All measurements were conducted in a low vacuum environment (50 Pa $\rm H_2O$ vapor) to mitigate sample charging. We note that such measurement conditions did not cause any observable sample degradation during measurement (over a week).

cAFM and KPFM. Conductive AFM and KPFM measurements were performed in an Oxford Instrument Asylum Research Cypher microscope with Budget Sensor Multi75E-G Cr/Pt coated AFM probes (~3 N/m). The Cypher microscope is equipped with a National Instrument DAQ card and LabView script for applying voltage and acquiring IV data. The automated experiment workflow is designed in a Python Jupyter Notebook.

ASSOCIATED CONTENT

Data Availability Statement

The method that supports the findings of this study is available at https://github.com/yongtaoliu/MHP GB by ResHedNet.

Supporting Information

The Supporting Information is available free of charge at https://pubs.acs.org/doi/10.1021/acsnano.3c03363.

NMF analysis of CL results (PDF)

AUTHOR INFORMATION

Corresponding Authors

Yongtao Liu — Center for Nanophase Materials Sciences, Oak Ridge National Laboratory, Oak Ridge, Tennessee 37830, United States; orcid.org/0000-0003-0152-1783; Email: liuy3@ornl.gov

Sergei V. Kalinin – Department of Materials Science and Engineering, University of Tennessee, Knoxville, Tennessee 37996, United States; orcid.org/0000-0001-5354-6152; Email: sergei2@utk.edu

Mahshid Ahmadi — Department of Materials Science and Engineering, University of Tennessee, Knoxville, Tennessee 37996, United States; orcid.org/0000-0002-3268-7957; Email: mahmadi3@utk.edu

Authors

Jonghee Yang — Department of Materials Science and Engineering, University of Tennessee, Knoxville, Tennessee 37996, United States; orcid.org/0000-0001-7013-6761

Benjamin J. Lawrie — Center for Nanophase Materials Sciences and Materials Science and Technology Division, Oak Ridge National Laboratory, Oak Ridge, Tennessee 37830, United States; orcid.org/0000-0003-1431-066X

Kyle P. Kelley – Center for Nanophase Materials Sciences, Oak Ridge National Laboratory, Oak Ridge, Tennessee 37830, United States; oorcid.org/0000-0002-7688-0484

Maxim Ziatdinov — Center for Nanophase Materials Sciences and Computational Sciences and Engineering Division, Oak Ridge National Laboratory, Oak Ridge, Tennessee 37830, United States; orcid.org/0000-0003-2570-4592

Complete contact information is available at: https://pubs.acs.org/10.1021/acsnano.3c03363

Author Contributions

Y.L. and S.V.K. conceived the project. M.Z. developed ensemble-ResHedNet. Y.L. implemented ensemble-ResHedNet in cAFM and obtained the results. J.Y. and A.M. synthesized the MHP film and conducted the CL measurement. All authors contributed to discussions and the final manuscript.

Notes

This manuscript has been authored by UT-Battelle, LLC, under Contract No. DE-AC0500OR22725 with the U.S. Department of Energy. The United States Government retains and the publisher, by accepting the article for publication, acknowledges that the United States Government retains a nonexclusive, paid-up, irrevocable, worldwide license to publish or reproduce the published form of this manuscript, or allow others to do so, for the United States Government purposes. The Department of Energy will provide public access to these results of federally sponsored research in accordance with the DOE Public Access Plan (http://energy.gov/ downloads/doe-public-access-plan). Paper preprint: Liu, Y.; Yang, J.; Lawrie, B. J.; Kelley, K. P.; Ziatdinov, M.; Kalinin, S. V.; and Ahmadi, M. Disentangling electronic transport and hysteresis at individual grain boundaries in hybrid perovskites via automated scanning probe microscopy. arXiv preprint, 2022, https://arxiv.org/abs/2210.14138 (accessed April 24, 2023).

The authors declare no competing financial interest.

ACKNOWLEDGMENTS

This effort (implementation in SPM, measurement, data analysis) was primarily supported by the center for 3D Ferroelectric Microelectronics (3DFeM), an Energy Frontier Research Center funded by the U.S. Department of Energy (DOE), Office of Science, Basic Energy Sciences under Award Number DE-SC0021118. Ensemble-ResHedNet, CL microscopy, and SPM experiments were done at the Center for Nanophase Materials Sciences (CNMS), which is a US Department of Energy, Office of Science User Facility at Oak Ridge National Laboratory. J.Y. and M.A. acknowledge support from National Science Foundation (NSF), Award Number No. 2043205. The authors acknowledge Rama K. Vasudevan for necessary developments for AE-SPM.

REFERENCES

- (1) National Renewable Energy Laboratory, Best Research-Cell Efficiency Chart. https://www.nrel.gov/pv/cell-efficiency.html (accessed April 2023).
- (2) Cheng, Y.; Ding, L. Pushing commercialization of perovskite solar cells by improving their intrinsic stability. *Energy Environ. Sci.* **2021**, *14* (6), 3233–3255.
- (3) Rong, Y.; Hu, Y.; Mei, A.; Tan, H.; Saidaminov, M. I.; Seok, S. I.; McGehee, M. D.; Sargent, E. H.; Han, H. Challenges for commercializing perovskite solar cells. *Science* **2018**, *361* (6408), eaat8235.
- (4) Park, N. G. Research direction toward scalable, stable, and high efficiency perovskite solar cells. *Adv. Energy Mater.* **2020**, *10* (13), 1903106.
- (5) Dasgupta, A.; Mahesh, S.; Caprioglio, P.; Lin, Y.-H.; Zaininger, K.-A.; Oliver, R. D.J.; Holzhey, P.; Zhou, S.; McCarthy, M. M.; Smith, J. A.; Frenzel, M.; Christoforo, M. G.; Ball, J. M.; Wenger, B.; Snaith, H. J. Visualizing macroscopic inhomogeneities in perovskite solar cells. *ACS Energy Letters* **2022**, *7* (7), 2311–2322.
- (6) Macpherson, S.; Doherty, T. A. S.; Winchester, A. J.; Kosar, S.; Johnstone, D. N.; Chiang, Y.-H.; Galkowski, K.; Anaya, M.; Frohna,

- K.; Iqbal, A. N.; Nagane, S.; Roose, B.; Andaji-Garmaroudi, Z.; Orr, K. W. P.; Parker, J. E.; Midgley, P. A.; Dani, K. M.; Stranks, S. D. Local nanoscale phase impurities are degradation sites in halide perovskites. *Nature* **2022**, *607* (7918), 294–300.
- (7) Frohna, K.; Anaya, M.; Macpherson, S.; Sung, J.; Doherty, T. A.; Chiang, Y.-H.; Winchester, A. J.; Orr, K. W.; Parker, J. E.; Quinn, P. D. Nanoscale chemical heterogeneity dominates the optoelectronic response of alloyed perovskite solar cells. *Nat. Nanotechnol.* **2022**, *17* (2), 190–196.
- (8) Szostak, R.; Silva, J.; Turren-Cruz, S.-H.; Soares, M.; Freitas, R.; Hagfeldt, A.; Tolentino, H.; Nogueira, A. Nanoscale mapping of chemical composition in organic-inorganic hybrid perovskite films. *Science advances* **2019**, *5* (10), eaaw6619.
- (9) Stranks, S. D. Multimodal microscopy characterization of halide perovskite semiconductors: Revealing a new world (dis) order. *Matter* **2021**, *4* (12), 3852–3866.
- (10) Kodur, M.; Kumar, R. E.; Luo, Y.; Cakan, D. N.; Li, X.; Stuckelberger, M.; Fenning, D. P. X-Ray microscopy of halide perovskites: techniques, applications, and prospects. *Adv. Energy Mater.* **2020**, *10* (26), 1903170.
- (11) Collins, L.; Ahmadi, M.; Qin, J.; Liu, Y.; Ovchinnikova, O. S.; Hu, B.; Jesse, S.; Kalinin, S. V. Time resolved surface photovoltage measurements using a big data capture approach to KPFM. *Nanotechnology* **2018**, *29* (44), 445703.
- (12) Hermes, I. M.; Bretschneider, S. A.; Bergmann, V. W.; Li, D.; Klasen, A.; Mars, J.; Tremel, W.; Laquai, F.; Butt, H.-J.; Mezger, M.; Berger, R.; Rodriguez, B. J.; Weber, S. A. L. Ferroelastic fingerprints in methylammonium lead iodide perovskite. *J. Phys. Chem. C* **2016**, *120* (10), 5724–5731.
- (13) Hermes, I. M.; Best, A.; Winkelmann, L.; Mars, J.; Vorpahl, S. M.; Mezger, M.; Collins, L.; Butt, H.-J.; Ginger, D. S.; Koynov, K.; Weber, S. A. L. Anisotropic carrier diffusion in single MAPbI 3 grains correlates to their twin domains. *Energy Environ. Sci.* **2020**, *13* (11), 4168–4177.
- (14) Taylor, E. J.; Iyer, V.; Dhami, B. S.; Klein, C.; Lawrie, B. J.; Appavoo, K. Hyperspectral nanoscale mapping of hybrid perovskite photophysics at the single grain level. *arXiv* 2022, preprint arXiv:2201.06546 (accessed April 2023).
- (15) Dhami, B. S.; Iyer, V.; Pant, A.; Tripathi, R. P.; Lawrie, B. J.; Appavoo, K. Angle-Resolved Cathodoluminescence Polarimetry of Hybrid Perovskites. *arXiv* 2022, preprint arXiv:2201.06484 (accessed April 2023).
- (16) Kutes, Y.; Zhou, Y.; Bosse, J. L.; Steffes, J.; Padture, N. P.; Huey, B. D. Mapping the photoresponse of CH3NH3PbI3 hybrid perovskite thin films at the nanoscale. *Nano Lett.* **2016**, *16* (6), 3434–3441.
- (17) Correa-Baena, J.-P.; Luo, Y.; Brenner, T. M.; Snaider, J.; Sun, S.; Li, X.; Jensen, M. A.; Hartono, N. T. P.; Nienhaus, L.; Wieghold, S.; Poindexter, J. R.; Wang, S.; Meng, Y. S.; Wang, T.; Lai, B.; Holt, M. V.; Cai, Z.; Bawendi, M. G.; Huang, L.; Buonassisi, T.; Fenning, D. P. Homogenized halides and alkali cation segregation in alloyed organic-inorganic perovskites. *Science* **2019**, *363* (6427), 627–631.
- (18) Kim, T.; Park, S.; Iyer, V.; Shaheen, B.; Choudhry, U.; Jiang, Q.; Eichman, G.; Gnabasik, R.; Kelley, K.; Lawrie, B.; Zhu, K.; Liao, B. Mapping the pathways of photo-induced ion migration in organic-inorganic hybrid halide perovskites. *Nat. Commun.* **2023**, *14* (1), 1846.
- (19) Liu, Y.; Borodinov, N.; Lorenz, M.; Ahmadi, M.; Kalinin, S. V.; Ievlev, A. V.; Ovchinnikova, O. S. Hysteretic ion migration and remanent field in metal halide perovskites. *Advanced Science* **2020**, 7 (19), 2001176.
- (20) Liu, Y.; Ievlev, A. V.; Borodinov, N.; Lorenz, M.; Xiao, K.; Ahmadi, M.; Hu, B.; Kalinin, S. V.; Ovchinnikova, O. S. Direct observation of photoinduced ion migration in lead halide perovskites. *Adv. Funct. Mater.* **2021**, *31* (8), 2008777.
- (21) Liu, Y.; Borodinov, N.; Collins, L.; Ahmadi, M.; Kalinin, S. V.; Ovchinnikova, O. S.; Ievlev, A. V. Role of decomposition product ions in hysteretic behavior of metal halide perovskite. *ACS Nano* **2021**, *15* (5), 9017–9026.

- (22) Kim, D.; Liu, Y.; Ievlev, A. V.; Higgins, K.; Ovchinnikova, O. S.; Yun, J. S.; Seidel, J.; Kalinin, S. V.; Ahmadi, M. Unraveling the hysteretic behavior at double cations-double halides perovskite-electrode interfaces. *Nano Energy* **2021**, *89*, 106428.
- (23) Rothmann, M. U.; Li, W.; Zhu, Y.; Bach, U.; Spiccia, L.; Etheridge, J.; Cheng, Y.-B. Direct observation of intrinsic twin domains in tetragonal CH3NH3PbI3. *Nat. Commun.* **2017**, 8 (1), 1–8.
- (24) Strelcov, E.; Dong, Q.; Li, T.; Chae, J.; Shao, Y.; Deng, Y.; Gruverman, A.; Huang, J.; Centrone, A. CH3NH3PbI3 perovskites: Ferroelasticity revealed. *Science advances* **2017**, 3 (4), e1602165.
- (25) Liu, Y.; Collins, L.; Proksch, R.; Kim, S.; Watson, B. R.; Doughty, B.; Calhoun, T. R.; Ahmadi, M.; Ievlev, A. V.; Jesse, S.; Retterer, S. T.; Belianinov, A.; Xiao, K.; Huang, J.; Sumpter, B. G.; Kalinin, S. V.; Hu, B.; Ovchinnikova, O. S. Chemical nature of ferroelastic twin domains in CH3NH3PbI3 perovskite. *Nature materials* **2018**, *17* (11), 1013–1019.
- (26) Liu, Y.; Collins, L.; Belianinov, A.; Neumayer, S. M.; Ievlev, A. V.; Ahmadi, M.; Xiao, K.; Retterer, S. T.; Jesse, S.; Kalinin, S. V.; Hu, B.; Ovchinnikova, O. S. Dynamic behavior of CH3NH3PbI3 perovskite twin domains. *Appl. Phys. Lett.* **2018**, *113* (7), 072102.
- (27) Huang, B.; Kong, G.; Esfahani, E. N.; Chen, S.; Li, Q.; Yu, J.; Xu, N.; Zhang, Y.; Xie, S.; Wen, H.; Gao, P.; Zhao, J.; Li, J. Ferroic domains regulate photocurrent in single-crystalline CH3NH3PbI3 films self-grown on FTO/TiO₂ substrate. *npj Quantum Materials* **2018**, 3 (1), 1–8.
- (28) Liu, Y.; Ievlev, A. V.; Collins, L.; Belianinov, A.; Keum, J. K.; Ahmadi, M.; Jesse, S.; Retterer, S. T.; Xiao, K.; Huang, J.; Sumpter, B. G.; Kalinin, S. V.; Hu, B.; Ovchinnikova, O. S. Strain-chemical gradient and polarization in metal halide perovskites. *Advanced Electronic Materials* **2020**, *6* (4), 1901235.
- (29) Xiao, X.; Li, W.; Fang, Y.; Liu, Y.; Shao, Y.; Yang, S.; Zhao, J.; Dai, X.; Zia, R.; Huang, J. Benign ferroelastic twin boundaries in halide perovskites for charge carrier transport and recombination. *Nat. Commun.* **2020**, *11* (1), 1–7.
- (30) Marçal, L. A.; Oksenberg, E.; Dzhigaev, D.; Hammarberg, S.; Rothman, A.; Björling, A.; Unger, E.; Mikkelsen, A.; Joselevich, E.; Wallentin, J. In situ imaging of ferroelastic domain dynamics in CsPbBr3 perovskite nanowires by nanofocused scanning X-ray diffraction. ACS Nano 2020, 14 (11), 15973–15982.
- (31) Liu, Y.; Trimby, P.; Collins, L.; Ahmadi, M.; Winkelmann, A.; Proksch, R.; Ovchinnikova, O. S. Correlating crystallographic orientation and ferroic properties of twin domains in metal halide perovskites. *ACS Nano* **2021**, *15* (4), 7139–7148.
- (32) Liu, Y.; Li, M.; Wang, M.; Collins, L.; Ievlev, A. V.; Jesse, S.; Xiao, K.; Hu, B.; Belianinov, A.; Ovchinnikova, O. S. Twin domains modulate light-matter interactions in metal halide perovskites. *APL Materials* **2020**, *8* (1), 011106.
- (33) Li, W.; Yadavalli, S. K.; Lizarazo-Ferro, D.; Chen, M.; Zhou, Y.; Padture, N. P.; Zia, R. Subgrain special boundaries in halide perovskite thin films restrict carrier diffusion. *ACS Energy Letters* **2018**, 3 (11), 2669–2670.
- (34) Zhang, S.; Han, G. Intrinsic and environmental stability issues of perovskite photovoltaics. *Progress in Energy* **2020**, *2* (2), 022002.
- (35) Rao, M. K.; Sangeetha, D.; Selvakumar, M.; Sudhakar, Y.; Mahesha, M. Review on persistent challenges of perovskite solar cells' stability. *Sol. Energy* **2021**, *218*, 469–491.
- (36) Bi, E.; Song, Z.; Li, C.; Wu, Z.; Yan, Y. Mitigating ion migration in perovskite solar cells. *Trends in Chemistry* **2021**, 3 (7), 575–588.
- (37) Zhang, T.; Hu, C.; Yang, S. Ion Migration: A "Double-Edged Sword" for Halide-Perovskite-Based Electronic Devices. *Small Methods* **2020**, *4* (5), 1900552.
- (38) Long, R.; Liu, J.; Prezhdo, O. V. Unravelling the effects of grain boundary and chemical doping on electron—hole recombination in CH3NH3PbI3 perovskite by time-domain atomistic simulation. *J. Am. Chem. Soc.* **2016**, *138* (11), 3884–3890.
- (39) Yun, J. S.; Ho-Baillie, A.; Huang, S.; Woo, S. H.; Heo, Y.; Seidel, J.; Huang, F.; Cheng, Y.-B.; Green, M. A. Benefit of grain

- boundaries in organic-inorganic halide planar perovskite solar cells. *Journal of Physical Chemistry Letters* **2015**, *6* (5), 875–880.
- (40) Park, J.-S.; Calbo, J.; Jung, Y.-K.; Whalley, L. D.; Walsh, A. Accumulation of deep traps at grain boundaries in halide perovskites. *ACS Energy Letters* **2019**, *4* (6), 1321–1327.
- (41) Qiao, L.; Fang, W.-H.; Long, R.; Prezhdo, O. V. Atomic model for alkali metal passivation of point defects at perovskite grain boundaries. *ACS Energy Letters* **2020**, *5* (12), 3813–3820.
- (42) Liu, Z.; Cao, F.; Wang, M.; Wang, M.; Li, L. Observing defect passivation of the grain boundary with 2-aminoterephthalic acid for efficient and stable perovskite solar cells. *Angew. Chem., Int. Ed.* **2020**, 59 (10), 4161–4167.
- (43) Liu, C.; Huang, Z.; Hu, X.; Meng, X.; Huang, L.; Xiong, J.; Tan, L.; Chen, Y. Grain boundary modification via F4TCNQ to reduce defects of perovskite solar cells with excellent device performance. ACS Appl. Mater. Interfaces 2018, 10 (2), 1909–1916.
- (44) Wang, C.; Song, Z.; Zhao, D.; Awni, R. A.; Li, C.; Shrestha, N.; Chen, C.; Yin, X.; Li, D.; Ellingson, R. J.; Zhao, X.; Li, X.; Yan, Y. Improving performance and stability of planar perovskite solar cells through grain boundary passivation with block copolymers. *Solar RRL* **2019**, *3* (9), 1900078.
- (45) Liu, W.; Liu, N.; Ji, S.; Hua, H.; Ma, Y.; Hu, R.; Zhang, J.; Chu, L.; Li, X. a.; Huang, W. Perfection of perovskite grain boundary passivation by rhodium incorporation for efficient and stable solar cells. *Nano-Micro Letters* **2020**, *12*, 1–11.
- (46) Yang, Y.; Wu, L.; Hao, X.; Tang, Z.; Lai, H.; Zhang, J.; Wang, W.; Feng, L. Beneficial effects of potassium iodide incorporation on grain boundaries and interfaces of perovskite solar cells. *RSC Adv.* **2019**, 9 (49), 28561–28568.
- (47) Ma, Y.; Zhang, H.; Zhang, Y.; Hu, R.; Jiang, M.; Zhang, R.; Lv, H.; Tian, J.; Chu, L.; Zhang, J.; Xue, Q.; Yip, H.-L.; Xia, R.; Li, X.; Huang, W. Enhancing the performance of inverted perovskite solar cells via grain boundary passivation with carbon quantum dots. *ACS Appl. Mater. Interfaces* **2019**, *11* (3), 3044–3052.
- (48) Leblebici, S. Y.; Leppert, L.; Li, Y.; Reyes-Lillo, S. E.; Wickenburg, S.; Wong, E.; Lee, J.; Melli, M.; Ziegler, D.; Angell, D. K.; Ogletree, D. F.; Ashby, P. D.; Toma, F. M.; Neaton, J. B.; Sharp, I. D.; Weber-Bargioni, A. Facet-dependent photovoltaic efficiency variations in single grains of hybrid halide perovskite. *Nature Energy* **2016**, *1* (8), 1–7.
- (49) Qin, T.-X.; You, E.-M.; Zhang, M.-X.; Zheng, P.; Huang, X.-F.; Ding, S.-Y.; Mao, B.-W.; Tian, Z.-Q. Quantification of electron accumulation at grain boundaries in perovskite polycrystalline films by correlative infrared-spectroscopic nanoimaging and Kelvin probe force microscopy. *Light: Science & Applications* **2021**, *10* (1), 1–8.
- (50) Saidaminov, M. I.; Williams, K.; Wei, M.; Johnston, A.; Quintero-Bermudez, R.; Vafaie, M.; Pina, J. M.; Proppe, A. H.; Hou, Y.; Walters, G.; Kelley, S. O.; Tisdale, W. A.; Sargent, E. H. Multication perovskites prevent carrier reflection from grain surfaces. *Nature materials* **2020**, *19* (4), 412–418.
- (51) Song, J.; Zhou, Y.; Padture, N. P.; Huey, B. D. Anomalous 3D nanoscale photoconduction in hybrid perovskite semiconductors revealed by tomographic atomic force microscopy. *Nat. Commun.* **2020**, *11* (1), 1–9.
- (52) Shao, Y.; Fang, Y.; Li, T.; Wang, Q.; Dong, Q.; Deng, Y.; Yuan, Y.; Wei, H.; Wang, M.; Gruverman, A.; Shield, J.; Huang, J. Grain boundary dominated ion migration in polycrystalline organic—inorganic halide perovskite films. *Energy Environ. Sci.* **2016**, 9 (5), 1752–1759.
- (53) Liu, Y.; Kelley, K. P.; Funakubo, H.; Kalinin, S. V.; Ziatdinov, M. Exploring physics of ferroelectric domain walls in real time: deep learning enabled scanning probe microscopy. *Advanced Science* **2022**, *9*, 2203957.
- (54) An, Y.; Perini, C. A. R.; Hidalgo, J.; Castro-Méndez, A.-F.; Vagott, J. N.; Li, R.; Saidi, W. A.; Wang, S.; Li, X.; Correa-Baena, J.-P. Identifying high-performance and durable methylammonium-free lead halide perovskites via high-throughput synthesis and characterization. *Energy Environ. Sci.* **2021**, *14* (12), 6638–6654.

- (55) Gharibzadeh, S.; Fassl, P.; Hossain, I. M.; Rohrbeck, P.; Frericks, M.; Schmidt, M.; Duong, T.; Khan, M. R.; Abzieher, T.; Nejand, B. A.; Schackmar, F.; Almora, O.; Feeney, T.; Singh, R.; Fuchs, D.; Lemmer, U.; Hofmann, J. P.; Weber, S. A. L.; Paetzold, U. W. Two birds with one stone: dual grain-boundary and interface passivation enables> 22% efficient inverted methylammonium-free perovskite solar cells. *Energy Environ. Sci.* 2021, 14 (11), 5875–5893.
- (56) Xie, S.; Tu, Z. Holistically-nested edge detection. *Proceedings of the IEEE International Conference on Computer Vision*; IEEE, 2015; pp 1395–1403.
- (57) Simonyan, K.; Zisserman, A. Very deep convolutional networks for large-scale image recognition. *arXiv* 2014, preprint arXiv:1409.1556 (accessed April 2023).
- (58) Liu, Y.; Proksch, R.; Wong, C. Y.; Ziatdinov, M.; Kalinin, S. V. Disentangling Ferroelectric Wall Dynamics and Identification of Pinning Mechanisms via Deep Learning. *Adv. Mater.* **2021**, 33 (43), 2103680.
- (59) Tsai, H.; Asadpour, R.; Blancon, J.-C.; Stoumpos, C. C.; Durand, O.; Strzalka, J. W.; Chen, B.; Verduzco, R.; Ajayan, P. M.; Tretiak, S.; Even, J.; Alam, M. A.; Kanatzidis, M. G.; Nie, W.; Mohite, A. D. Light-induced lattice expansion leads to high-efficiency perovskite solar cells. *Science* **2018**, *360* (6384), 67–70.
- (60) Li, Y.-T.; Ding, L.; Li, J.-Z.; Kang, J.; Li, D.-H.; Ren, L.; Ju, Z.-Y.; Sun, M.-X.; Ma, J.-Q.; Tian, Y.; Gou, G.-Y.; Xie, D.; Tian, H.; Yang, Y.; Wang, L.-W.; Peng, L.-M.; Ren, T.-L. Light-enhanced ion migration in two-dimensional perovskite single crystals revealed in carbon nanotubes/two-dimensional perovskite heterostructure and its photomemory application. ACS central science 2019, 5 (11), 1857—1865.
- (61) Liu, Y.; Sumpter, B. G.; Keum, J. K.; Hu, B.; Ahmadi, M.; Ovchinnikova, O. S. Strain in metal halide perovskites: the critical role of A-site cation. *ACS Applied Energy Materials* **2021**, 4 (3), 2068–2072.
- (62) Liu, Y.; Ievlev, A. V.; Collins, L.; Borodinov, N.; Belianinov, A.; Keum, J. K.; Wang, M.; Ahmadi, M.; Jesse, S.; Xiao, K.; Sumpter, B. G.; Hu, B.; Kalinin, S. V.; Ovchinnikova, O. S. Light-ferroic interaction in hybrid organic—inorganic perovskites. *Advanced Optical Materials* **2019**, *7* (23), 1901451.
- (63) Ni, Z.; Xu, S.; Jiao, H.; Gu, H.; Fei, C.; Huang, J. High grain boundary recombination velocity in polycrystalline metal halide perovskites. *Science advances* **2022**, *8* (36), eabq8345.
- (64) Wang, Y.; Fang, W.-H.; Long, R.; Prezhdo, O. V. Symmetry breaking at MAPbI3 perovskite grain boundaries suppresses charge recombination: Time-domain ab initio analysis. *J. Phys. Chem. Lett.* **2019**, *10* (7), 1617–1623.
- (65) Wu, H.; Xu, C.; Zhang, Z.; Xiong, Z.; Shi, M.; Ma, S.; Fan, W.; Zhang, Z.; Liao, Q.; Kang, Z.; Zhang, Y. Omnibearing Interpretation of External Ions Passivated Ion Migration in Mixed Halide Perovskites. *Nano Lett.* **2022**, 22 (4), 1467–1474.
- (66) Hu, Z.; An, Q.; Xiang, H.; Aigouy, L.; Sun, B.; Vaynzof, Y.; Chen, Z. Enhancing the efficiency and stability of triple-cation perovskite solar cells by eliminating excess PbI2 from the perovskite/hole transport layer interface. ACS Appl. Mater. Interfaces 2020, 12 (49), 54824–54832.
- (67) Roose, B.; Dey, K.; Chiang, Y.-H.; Friend, R. H.; Stranks, S. D. Critical assessment of the use of excess lead iodide in lead halide perovskite solar cells. *J. Phys. Chem. Lett.* **2020**, *11* (16), 6505–6512. (68) Shan, D.; Tong, G.; Cao, Y.; Tang, M.; Xu, J.; Yu, L.; Chen, K. The effect of decomposed PbI2 on microscopic mechanisms of scattering in CH3NH3PbI3 films. *Nanoscale Res. Lett.* **2019**, *14* (1), 1–6
- (69) Chen, Y.; Meng, Q.; Xiao, Y.; Zhang, X.; Sun, J.; Han, C. B.; Gao, H.; Zhang, Y.; Lu, Y.; Yan, H. Mechanism of PbI₂ in situ passivated perovskite films for enhancing the performance of perovskite solar cells. ACS Appl. Mater. Interfaces 2019, 11 (47), 44101–44108.
- (70) Shi, B.; Yao, X.; Hou, F.; Guo, S.; Li, Y.; Wei, C.; Ding, Y.; Li, Y.; Zhao, Y.; Zhang, X. Unraveling the passivation process of PbI2 to

- enhance the efficiency of planar perovskite solar cells. *J. Phys. Chem. C* **2018**, 122 (37), 21269–21276.
- (71) Xiao, C.; Li, Z.; Guthrey, H.; Moseley, J.; Yang, Y.; Wozny, S.; Moutinho, H.; To, B.; Berry, J. J.; Gorman, B.; Yan, Y.; Zhu, K.; Al-Jassim, M. Mechanisms of electron-beam-induced damage in perovskite thin films revealed by cathodoluminescence spectroscopy. *J. Phys. Chem. C* **2015**, *119* (48), 26904–26911.
- (72) Taylor, E. J.; Iyer, V.; Dhami, B. S.; Klein, C.; Lawrie, B. J.; Appavoo, K. Hyperspectral nanoscale mapping of hybrid perovskite photophysics at the single grain level. *arXiv* 2022, preprint arXiv:2201.06546 (accessed April 2023).
- (73) Guthrey, H.; Moseley, J. A review and perspective on cathodoluminescence analysis of halide perovskites. *Adv. Energy Mater.* **2020**, *10* (26), 1903840.